Continuous vs. discontinuous garnet growth in mylonitic micaschists from northeastern Sardinia, Italy: Evidence from LA-ICPMS trace element mapping

Gabriele Cruciani [a], Dario Fancello [a], Marcello Franceschelli [a,*], Daniela Rubatto [b]

[a] *Dipartimento di Scienze Chimiche e Geologiche, Università degli Studi di Cagliari, Italy*
[b] *Institute of Geological Sciences, Universität Bern, Switzerland*

A B S T R A C T

Garnet with complex, discontinuous zoning is a common occurrence in metamorphic terrains, and the relationship between major and trace element zoning can provide insight into the metamorphic evolution of the host rock. Mylonitic micaschists along the Posada-Asinara Shear Zone in the Axial Zone of the Sardinia Variscan chain contain garnet porphyroblasts, enveloped by the S2 schistosity, with distinct core and rim domains. A large garnet porphyroblasts was investigated by laser ablation-inductively coupled plasma-mass spectrometry (LA-ICPMS) mapping. The major element compositional variation follows a bell-shaped zoning, with Ca and Mn contents progressively decreasing, and Fe and Mg increasing, from the core to the outer rim. LA-ICPMS mapping revealed a thin and sharp annular enrichment zone in Y, Sc, Dy, Ho, Er, Tm at the mantle-rim boundary. The trace element (TE) compositional profiles show a central enrichment area for HREE (Tm, Yb, Lu). This enrichment decreases progressively, as a function of atomic number, for Er, Ho and Dy. Elements with even lower atomic number (Tb, Gd, Eu and Sm), are depleted in this central domain, but their content increases in broad shoulders towards the garnet rim. The position of these lateral shoulders migrates progressively rimwards with decreasing atomic number. The REE distribution, trend and behavior in the growth zones of the garnet is an example of TE control during a continuous growth ruled by diffusion-limited REE uptake. The Y + HREE annular enrichment zone, interpreted as resulting from a decrease in the garnet growth rate, reflects a short-lived episode in the garnet growth history.

1. Introduction

Garnet is an invaluable mineral for understanding the history and evolution of metamorphic rocks. It is a rock-forming mineral in the upper mantle and continental crust, and it is stable from the greenschist to the UHP eclogite and UHT granulite metamorphic facies. Garnet has long been used to study a wide range of thermobaric conditions through the calibration of the garnet-biotite thermometer and the GASP geobarometer (Ferry and Spear, 1978; see Wu and Cheng, 2006 for a review). Valuable information on the history of metamorphic rocks, with particular reference to the generally hidden prograde part of the P-T path, is also obtained by studying the compositional zoning of garnet and the nature and distribution of its inclusion pattern. Garnet is also known to be resistant to re-equilibration, making it a good recorder of polymetamorphism (e.g. Baxter et al., 2017 and references therein). Last

but not least, recent analytical improvements in garnet dating (e.g. Sm-Nd: Pollington and Baxter, 2011; U-Pb: Seman et al., 2017; Millonig et al., 2020; Lu-Hf: Simpson et al., 2021, 2023; Tual et al., 2022; Sm—Nd and Lu-Hf: Smit et al., 2013) provide new opportunities to date the evolution and rate of various geological processes, while oxygen isotope zoning in garnet is the new frontier in exploring fluid/melt-rock interactions at depth (e.g. Bovay et al., 2021a; Higashino et al., 2019; Page et al., 2014; Raimondo et al., 2012).

Numerous studies have shown that a full understanding of garnet growth zoning is fundamental for the application of thermodynamic modelling in reconstructing the P-T evolution of metamorphic rocks (e. g. Cao et al., 2017; Giuntoli et al., 2018; Thiessen et al., 2019; Bovay et al., 2021b; Kulhánek et al., 2021; Kulhánek and Faryad, 2023). The relatively slow diffusivity of TE in garnet allows the preservation of growth zones resulting from complex metamorphic evolutions (George

---

* Corresponding author.
E-mail address: francmar@unica.it (M. Franceschelli).

et al., 2018 and references therein). Recent improvements in TE mapping techniques, as well as in the resolution and accuracy of their results, allow to have a clear view of the very fine zoning microstructures preserved within the garnet porphyroblasts (George et al., 2018; Konrad-Schmolke et al., 2023; Raimondo et al., 2017; Rubatto et al., 2020; Tual et al., 2022).

We highlight that several processes control TE incorporation and distribution in garnet, including: (i) local availability and breakdown of mineral phases; (ii) inheritance and redistribution with included or nearby phases; (iii) diffusion-limited availability of TE (with particular reference to REE). We also investigate the role and extent to which TE uptake in garnet is controlled by the mineral reaction history. Finally, our case study where major element zoning in garnet is continuous and TE is not, emphasizes that the comparison between major and trace element compositional zoning is a powerful tool to discriminate between polycyclic and continuously growing garnet.

2. Geological setting and field geology

The metamorphic basement of Sardinia consists of a stack of S- to SW-verging tectonic units with increasing metamorphic grade from SW to NE subdivided into the External Zone, the Nappe Zone (in turn subdivided into Internal and External Nappe) and the Inner Zone (Carmignani et al., 2001 and references therein). The metamorphic sequences exposed in the External and Nappe Zones underwent anchizone to greenschist facies conditions, with the exception of the Capo Spartivento (SW Sardinia) metamorphic rocks and the Monte Grighini Unit (in the Nappe Zone), which record amphibolite-facies P-T conditions (Cruciani et al., 2016, 2018, 2019).

The Inner Zone covers northern Sardinia and southern Corsica (Cruciani et al., 2021; Massonne et al., 2018). In NE Sardinia, the Inner Zone consists of the Medium-Grade Metamorphic Complex (MGMC) and High-Grade Metamorphic Complex (HGMC, also known as Migmatite Complex) separated by the Posada-Asinara Shear Zone (PASZ). This shear zone was active at ~325–300 Ma in a transpressive tectonic setting, in agreement with the ages of the other shear zones in the southern Variscan belt (Carosi et al., 2020; Carosi and Palmeri, 2002). South of the PASZ, the MGMC consists of micaschist and paragneiss, locally with relics of HP assemblages (Cruciani et al., 2022) with intercalated quartzite, metabasite and orthogneiss (Helbing and Tiepolo, 2005).

The Migmatite Complex (HGMC) consists of gneisses and HP migmatites of igneous and sedimentary origin (Fancello et al., 2018 and references therein) with calc-silicate nodules, layered amphibolites resembling leptyno-amphibolite, and metabasite with eclogite- and granulite-facies mineral relics (Scodina et al., 2019, 2020, 2021).

Polyphase ductile deformation in northern Sardinia has been described by several authors (Carosi et al., 2020; Carosi and Palmeri, 2002; Connolly et al., 1994; Franceschelli et al., 1982; Helbing et al., 2006). In micaschists from the garnet zone of NE Sardinia, the first deformation D1 (~345–340 Ma, Di Vincenzo et al., 2004) is associated with shearing and folding associated with a pervasive S1 axial plane foliation in some areas of the MGMC. The S1 foliation is progressively transposed to the north by the D2 phase. The Variscan D2 transpressive shear is the main deformation observed in northern Sardinia (Carosi and Palmeri, 2002), associated with upright up to NE-verging folds and dextral shear zones. Di Vincenzo et al. (2004) found apparent $^{40}Ar—^{39}Ar$ ages of 320–305 Ma for most syn–D2 white mica in the MGMC. Carosi et al. (2020) used in situ U-Th-Pb ages on zircon and monazite in mylonitic rocks to show that the PASZ was active at ~325–300 Ma in a transpressive setting. Subsequently, D3 deformation developed forming upright metric to decametric open folds. F3 folds are associated with an S3 axial plane crenulation cleavage. The D4 tectonic phase is revealed by metric to decametric folds with subhorizontal axial planes (Cruciani et al., 2015).

The studied rocks (40°36′17″N, 9°35′29″E) outcrop to the north of the SP50 road connecting the village of S. Anna (to the east) and Lodè (to the west) in the south-eastern sector of the PASZ. The Variscan metamorphic rocks consist mainly of micaschist and paragneiss. Granodioritic orthogneiss and augen gneiss crop out in the southern sector of the study area, while amphibolite lenses, embedded in the metasedimentary sequence of the kyanite + biotite zone, are aligned along the PASZ a few kilometers north of the study area. Silver-colored mylonitic micaschists (Fig. 1a) characterized by the occurrence of abundant garnet crystals visible to the naked eye, were collected in the forest near a small traditional building known as "Su Pinnettu".

3. Methods

Single spot analyses of Sc, Ti, V, Cr, Y, Zr, Nb, Hf, Ta, Pb, Th, U and REE in garnet, staurolite, chloritoid, biotite, muscovite and plagioclase were acquired at the University of Cagliari using a quadrupole inductively coupled plasma-mass spectrometer (ICP-MS) Perkin Elmer Elan DRC-e coupled to a 213 nm Nd:YAG laser probe manufactured by New Wave Research. Measurements were made with 46–50 mJ laser energy, spot sizes of 65 μm, a pulse energy of 0.2 mJ, a repetition rate of 7 Hz, 50–60 s ablation, 60 s background and 30 s washout delay. Analyses were calibrated against the silicate glass reference material NIST SRM 612 and the glass BCR-2G was measured as an unknown to monitor accuracy. Data reduction was made with the software Glitter (Griffin et al., 2008) using ^{29}Si as internal standard in concentrations determined by electron microprobe.

Major, minor and trace element maps of garnet were obtained by LA-ICP-MS using a Resonetics RESOlutionSE 193 nm excimer laser system equipped with an S-155 large volume constant geometry cell (Laurin Technic, Australia) at the Institute of Geological Sciences, University of Bern, Switzerland. The laser system is coupled to an Agilent 7900 quadrupole ICP- MS instrument that was tuned for low oxide production (ThO/Th <0.2%) and Th/U ratio close to unity (Th/U > 97%). Mapping was performed on a regular 30 μm thick polished thin section by scanning with a 16 μm spot at a scan speed of 25 μm/s, after pre-ablation to minimize the effect of redeposition. Ablation was performed in an atmosphere of He (0.7 L/min) and N_2 (0.003 L/min) mixed with Ar (0.86 L/min) immediately after the ablation cell. A laser repetition rate of 10 Hz and a fluence on sample of 7 J/cm^2 were used. Data acquisition was performed in time-resolved analysis mode as a single continuous experiment. Background (60 s) and primary standard GSD-1 g were analyzed every 15 min, secondary standard SRM- NIST 612 every 30 min with the same scanning conditions. The analysis run table included a series of 38 elements from Li to U, for a total sweep time of 0.53. Data reduction was performed using the XMap Tools 4.1 software (Lanari and Piccoli, 2020). Instrument drift and mass bias were corrected for by applying a linear fit to the data set of standards. Quantification was performed using Si for internal calibration.

4. Petrography

The studied schist sample (specimen FZ13) is a silver colored, foliated mylonitic rock with reddish/brownish garnet peciloblasts up to 1.5 cm in size associated with plagioclase and staurolite porphyroblasts, with quartz, biotite, white mica, chloritoid and chlorite in the matrix (Fig. 1a). The modal abundances are: plagioclase (10 vol%), quartz (25 vol%), garnet (15 vol%), biotite (10 vol%), staurolite (up to 10 vol%), muscovite (30 vol%), and minor chloritoid and chlorite.

Two garnet porphyroblasts were studied in detail (Fig. 1b,c): the first one (Grt1) is slightly elongated (about 7 mm long), oriented along the S2 foliation and characterized by an inclusion-rich core surrounded by an inclusion-free, strongly fractured rim. The second one (Grt2) is rounded, approximately 6 mm in diameter, with an inclusion-rich core surrounded by a rim almost free of inclusions. In both porphyroblasts, the garnet core contains numerous inclusions of quartz, rutile, apatite, monazite and zircon that define a S1 foliation with a "snowball garnet"
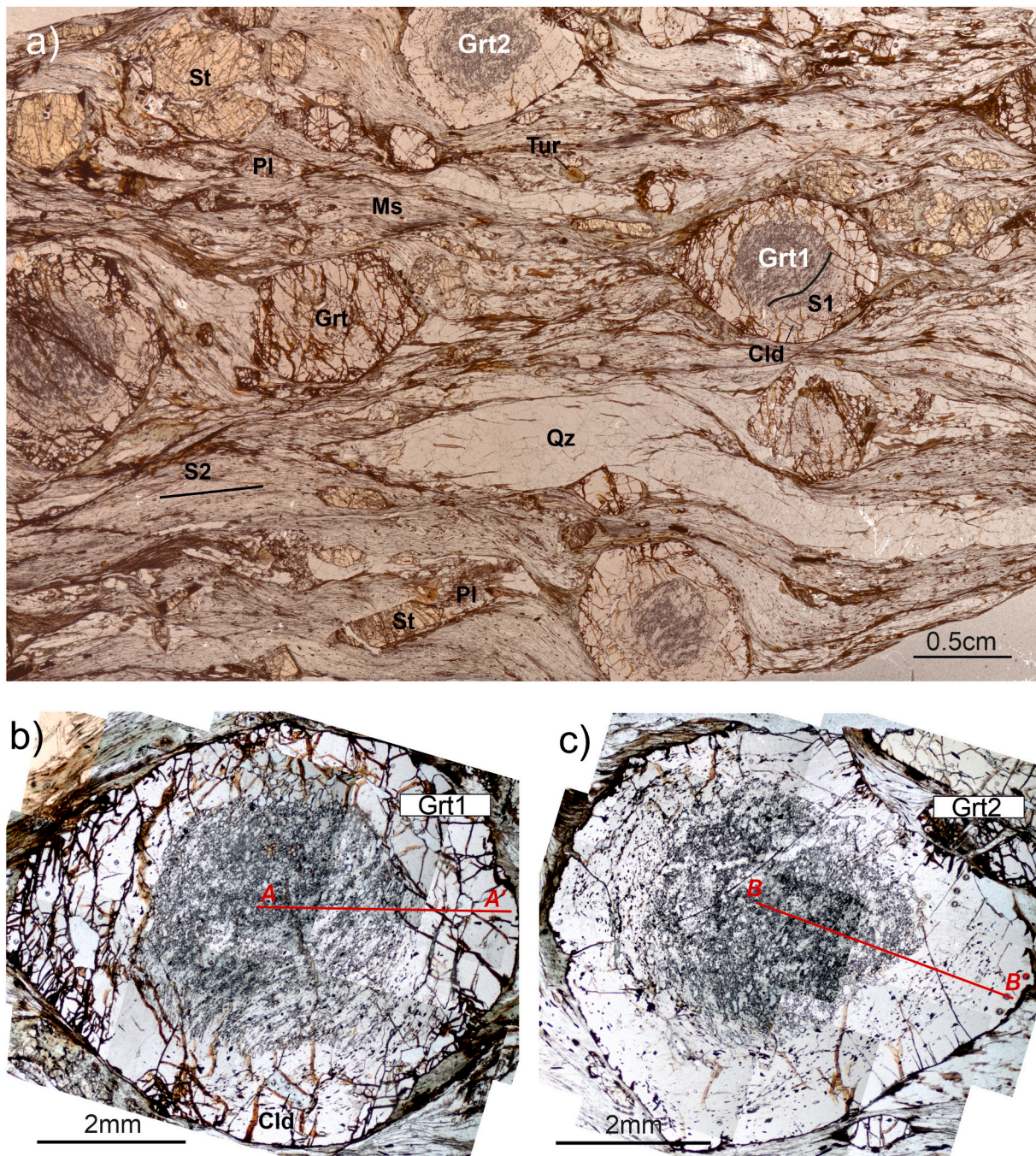
Fig. 1. (a) Thin section photo-scan of sample FZ13 (modified from Cruciani et al., 2022). Grt1 major element zoning, TE point analyses and TE mapping are given in this paper; For Grt2, major element zoning is given in Cruciani et al. (2022) and TE point analyses in this paper; (b), (c) photomicrographs showing the micro-structure of the two garnet crystals (Grt1 and Grt2) investigated in this study. A-A′, B-B′: traces of compositional profiles in Figs. 3 and A1, respectively. The two garnet crystals are localized at the thin section scale in (a). Mineral abbreviations after Whitney and Evans (2010).

microstructure. Rutile inclusions are present only in the garnet core and are sporadically associated with (and/or partially replaced by) ilmenite. Inclusions that were observed only in the rim domain are ilmenite, chloritoid and staurolite.

The staurolite porphyroblasts (up to 0.5 cm long) contain rounded quartz inclusions, euhedral tourmaline inclusions, elongated and oriented ilmenite microcrystals and accessory monazite and zircon. These porphyroblasts appear highly fractured, surrounded by chlorite and/or characterized by chlorite overgrowth along veins and fractures.

Chloritoid, found only as inclusions in garnet, is associated with paragonite and sporadically with margarite or traces of corundum.

Paragonite grows at the expense of chloritoid, whereas margarite and corundum only occur at the interface between chloritoid and garnet. A prismatic, rectangular, greenish chloritoid inclusion is clearly visible in the lower rim of Grt1, even under polarizing light (Fig. 1a,b). Within the plagioclase, a faint pre-D2 relic foliation is identified by a weak orientation of muscovite flakes, at a high angle with respect to S2 rock foliation. Potassic white mica is included in garnet and plagioclase, while paragonite, which is strictly associated with chloritoid, was observed only included in garnet.

The clockwise P-T path of the schist consists of a prograde segment followed by an increase in temperature of about 100 °C (from 500 to

600 °C) after the peak pressure until the peak conditions in the staurolite field (Cruciani et al., 2022). Peak pressure and temperature are diachronous, as the temperature increase is accompanied by a significant pressure decrease of at least 1.0 GPa (from 1.7 to 0.7 GPa). Further details on the microstructure and mineral assemblages of the sample studied are given by Cruciani et al. (2022).

5. Mineral chemistry

5.1. Major elements in garnet

Representative major element analyses from the core, mantle, inner and outer rim of the Grt1 crystal shown in Fig. 1b are reported in Table 1, while Mg, Ca, Mn, Fe compositional maps for the same garnet are shown in Fig. 2. For Grt2, major element analyses along with Mg, Ca, Mn, Fe compositional maps are given in Cruciani et al. (2022).

The Mg, Ca, Mn, Fe mapping of Grt1 confirms that four distinct growth zones (core, mantle, inner rim and outer rim, see Fig. 2) can be identified in the garnet porphyroblasts of sample FZ13, as already proposed by Cruciani et al., (2022, see their Fig. 4a). Major element compositional variation follows a bell-shaped zoning (Fig. 3 and A1 of Supplementary Material), with Ca and Mn contents progressively decreasing, and Fe and Mg increasing, from the core domain to the outer rim. The composition of the garnet Grt1 (Table 1) is $Alm_{45}Grs_{25}Prp_1Sps_{29}$ (core), $Alm_{66}Grs_{14}Prp_3Sps_{18}$ (mantle), $Alm_{84}Grs_7Prp_6Sps_3$ (rim), $Alm_{86}Grs_3Prp_{11}Sps_1$ (outer rim).

5.2. Trace elements in garnet

Representative TE analyses from the four growth zones of Grt1 and Grt2 are listed in Table 2. Compositional profiles of TE from core to rim of Grt1 and LA-ICPMS TE concentration maps are shown in Figs. 4 and 5, 6, respectively.

Despite the relatively simple (and typical) bell-shaped major element zoning, TE show a more complex compositional pattern. A striking feature revealed by LA-ICPMS mapping is a thin and sharp *annulus* enriched in Y, Sc, Tb, Dy, Ho, Er, Tm, Yb, Lu at the mantle-rim boundary of Grt1, with concentrations reaching up to 657 μg/g for Y and 106 μg/g for Dy (Fig. 4). Despite some scatter and enrichment of some elements in fractures or micro inclusions, the TE profiles, show an overall rimwards decreasing trend for V, Nb, Ta, Yb and Lu. For example, V decreases from

93 to 84 to 35–16 μg/g, Nb from 6 to 3 to 0.12 μg/g, Yb from 79 to 67 to 0.26 μg/g and Lu from 11 to 0.08 μg/g from core to rim (see Table 2). Y and to a lesser extent Ti also show such a trend, with an additional Y peak at the mantle-rim interface (i.e. *annulus*). In addition to the core to rim zoning, the TE map better shows the details and irregularities of the zoning pattern (Figs. 5,6). Sc, Y and the HREE show an asymmetric distribution in the core, where the SE quadrant is relatively enriched with respect to the others. V is highest in the core of the garnet and shows a weak oscillatory zoning in the rim. Cr appears to be enriched in the lower part of the inner rim near a chloritoid inclusion (Fig. 5); this zoning is not reflected by any other elements. Nb shows a concentric, bell-shaped zoning with progressive depletion from core to rim. Elements that are relatively incompatible in garnet (Zr, Hf, Th and U are mostly below detection limits in both spot analysis and maps, Table 2) or show sporadic spikes (Fig. 4), possibly indicating incidental ablation of micro inclusions of accessory phases (such as zircon, monazite, etc.). LREE (from La to Nd) are below the limit of detection for the maps.

The detectable REE (Sm to Lu) have different zoning that follow a trend from light to heavy (Fig. 4). Sm, Eu and Gd are depleted in the core and in the *annulus,* and their concentration increases in the inner rim just outside the *annulus* to drop again in the outer rim; Tb to Ho are low in the core, gradually increase outward in the mantle to reach their highest concentration in the *annulus*, then decrease in the inner rim towards a relatively sharp boundary with a TE-poor outer rim. Elements from Tm to Lu have high concentrations in the inner core, another peak in the asymmetric inner part of the mantle and reach their highest (not for Lu) content in the *annulus,* and their concentration drops to very low values in the rim. In summary, excluding the *annulus* that is enriched in most M-HREE and Y, the peak of concentrations in the REE shifts from core to inner rim with decreasing atomic number.

The described changes in REE concentrations result in different chondrite-normalized REE patterns between the different garnet growth zones (Fig. 7). The REE patterns were measured by spot analysis in the different growth zones of Grt1 and Grt2 (Fig. 7). Those of the garnet core are steep and strongly fractionated (with HREE abundances up to 1000 times the chondrite values), whereas those of the outer rims are flatter, slightly concave and with HREE between 1 and 10 times the chondrite values. The garnet mantle and inner rim show an intermediate REE fractionation between that of the core and the outer rim. The patterns of the inner rim also show a pronounced increase in MREE with respect to the HREE.

5.3. Other minerals

Cr and V contents in staurolite porphyroblasts range between 80 and 124 and 96–108 μg/g, respectively (Table A1). The $\sum$REE in staurolite is low (0.2–0.4 μg/g). The only significant TE variation from core to rim is observed for Cr (from 124 μg/g in the core to 80–100 μg/g in the rim).

Chloritoid has very low (< 1 μg/g) TE contents except for Sc (6 μg/g), V (122–137 μg/g), Cr (42–78 μg/g) and Ti (10 μg/g) in one of two chloritoid analyses. Biotite contains significant amounts of Sc (7–11 μg/g), Ti (709–764 μg/g), V (112–118 μg/g), Cr (28–46 μg/g), Rb (468–501 μg/g) and Ba (206–214 μg/g). The $\sum$REE in biotite is low (>4 μg/g). Chondrite-normalized REE patterns (Fig. A2) show relatively flat REE contents ranging from 0.1 to 10 times the chondrite values with a slight negative Eu anomaly. The TE content of plagioclase is restricted to Rb (17 μg/g), Sr (129 μg/g) and Ba (86 μg/g). The $\sum$REE in plagioclase is 6 μg/g. The chondrite-normalized REE pattern is poorly fractionated with a weak positive Eu anomaly (Fig. A2).

Monazite composition in the studied sample has been reported by Cruciani et al. (2022). X-ray compositional maps for Y, Ce, and Th of two monazite grains, one included in garnet and one from the rock matrix, are given in the Supplementary Fig. A3. Compositional X-ray maps, show that Y content increases from the core to the thin and discontinuous rim (0.01 to 0.30 wt% Y_2O_3). The Ce content (~ 30 wt% Ce_2O_3) is constant through the grains, while Th (2–6 wt% ThO_2) slightly increases

Table 1
Representative electron microprobe analyses (wt%) of the core, mantle, rim and outer rim of Grt1 and Grt2 from sample FZ13.

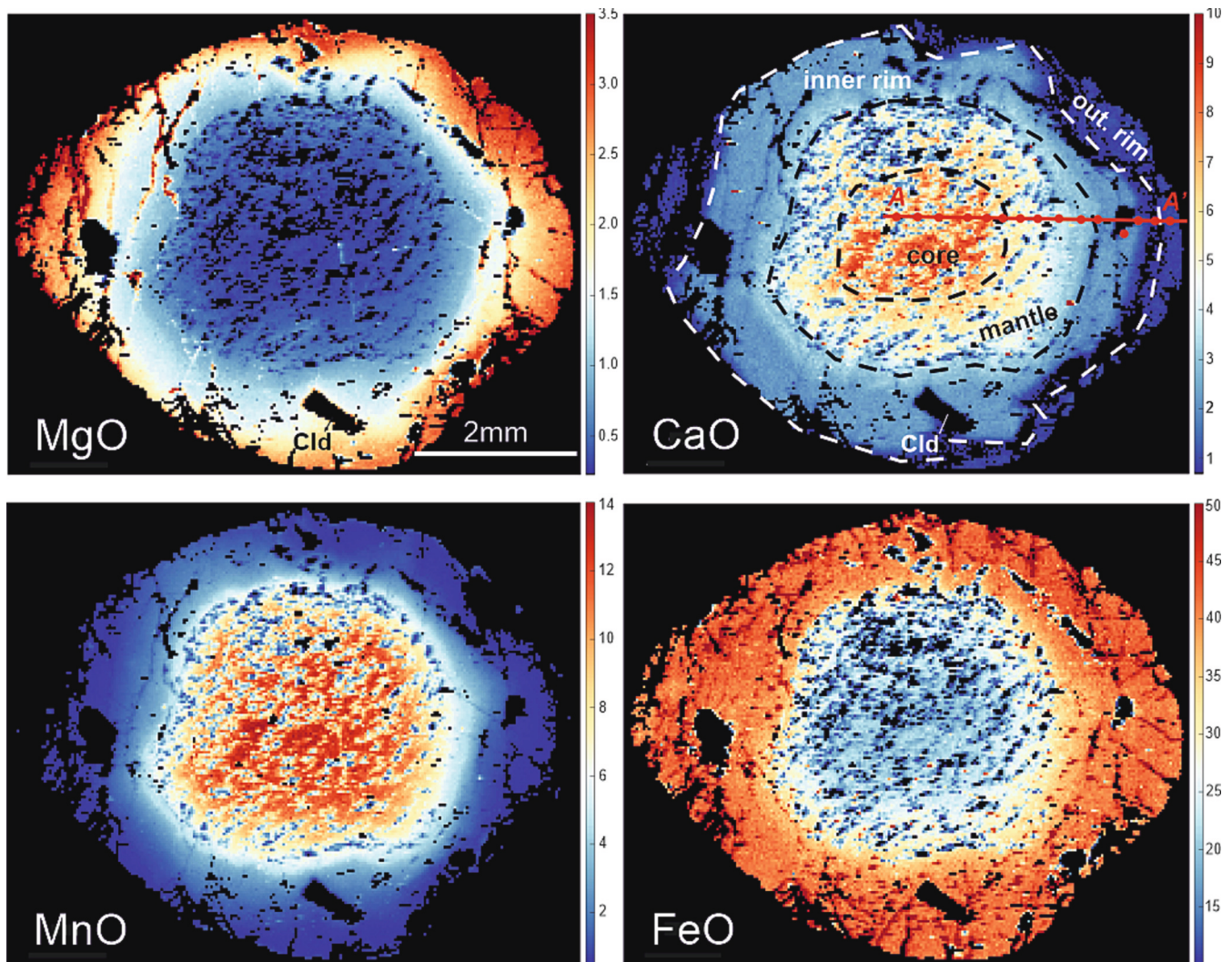|	core	mantle	inner rim	out. rim
SiO_2	36.74	36.60	36.64	37.13
TiO_2	0.21	0.13	0.06	0.03
Al_2O_3	20.87	20.67	20.71	21.26
FeO	20.53	29.73	37.95	39.17
Cr_2O_3	0.01	0.01	–	–
MnO	13.10	8.04	1.23	0.33
MgO	0.32	0.67	1.56	2.83
CaO	8.89	4.83	2.27	0.90
Tot	100.67	100.68	100.42	101.65
Oxy	12	12	12	12
Si	2.96	2.97	2.98	2.97
Al	1.98	1.98	1.99	2.00
Ti	0.01	0.01	0.00	0.00
Fe^{2+}	1.38	2.02	2.58	2.62
Cr	0.00	0.00	–	–
Mn	0.89	0.55	0.09	0.02
Mg	0.04	0.08	0.19	0.34
Ca	0.77	0.42	0.20	0.08
Alm	45	66	84	86
Prp	1	3	6	11
Grs	25	14	7	3
Sps	29	18	3	1

Fig. 2. X-ray major element (MgO, CaO, MnO and FeO) concentration maps (wt%) of the Grt1 porphyroblast shown in Fig. 1b. A-A' trace in the calcium map show the measuring points for the compositional profiles in Fig. 3.

from core to rim. In one crystal, a thin, Th-poor outer rim was observed.

6. Discussion

Trace element and REE distribution along the profile of metamorphic garnets has been explained in literature by the following different processes such as Rayleigh fractionation, diffusion-limited uptake, major- (and/or accessory) phases breakdown, inheritance from previous phases, and *syn-* to post-growth intracrystalline diffusion (e.g. George et al., 2018; Hirsch et al., 2003; Konrad-Schmolke et al., 2008; Moore et al., 2013; Otamendi et al., 2002; Pyle and Spear, 1999; Raimondo et al., 2017; Skora et al., 2006; Yang and Rivers, 2002). Each of these processes has implication for garnet petrogenesis and P-T evolution.

Below we discuss the TE zoning in the studied garnet and its significance for TE incorporation and distribution and for the P-T evolution of the sample. The metamorphic evolution of the studied mylonitic schists has been investigated by Cruciani et al. (2022), who defined the garnet growth P-T trajectory on the basis of the garnet major component zoning trend by using the Compositional Zoning in Garnet and its Modification by diffusion (CZGM) software by Faryad and Ježek (2019) and Faryad et al. (2022). The clockwise P-T path is divided into two different stages, separately for the core and rim profile: the first stage is recorded by the compositional variation of garnet from core to mantle, while the second one reflects garnet rim growth during exhumation. The garnet core +

mantle growth occurred along stage (a) of the P-T path shown in Fig. 8 whereas the rim growth occurred along stage (b), which was calculated after fractionation of the core + mantle. Representative isomode (vol%) of garnet, chloritoid, staurolite and biotite are given in Fig. 8. See below (section 6.2) for discussion on polymetamorphism vs. single tectonic cycle.

6.1. Rayleigh fractionation vs. diffusion-controlled REE uptake

Small to moderate amounts of garnet growing along a prograde trajectory of the P-T field in equilibrium with a large volume of reacting rock develop, at least for compatible elements such as Y + HREE, a Rayleigh fractionation profile resulting in a progressive, "bell-shaped" profile along a rim-core-rim transect (e.g., Gieré et al., 2011; Moore et al., 2013; Otamendi et al., 2002). Although bell-shaped profiles are observed for major components in the two garnet grains studied (Figs. 2,3), this was not observed for compatible TE. Only relatively incompatible elements such as V, Nb, Ta shows such a trend, whereas Y + HREE have a more complex zoning.

As previously described, the general trend of REE is an outward increase in content with decreasing atomic number, coupled with an annular enrichment of M-HREE at the mantle-rim transition. This distribution cannot be explained by a simple Rayleigh fractionation process, where a bell-shaped profile is expected due to the progressive
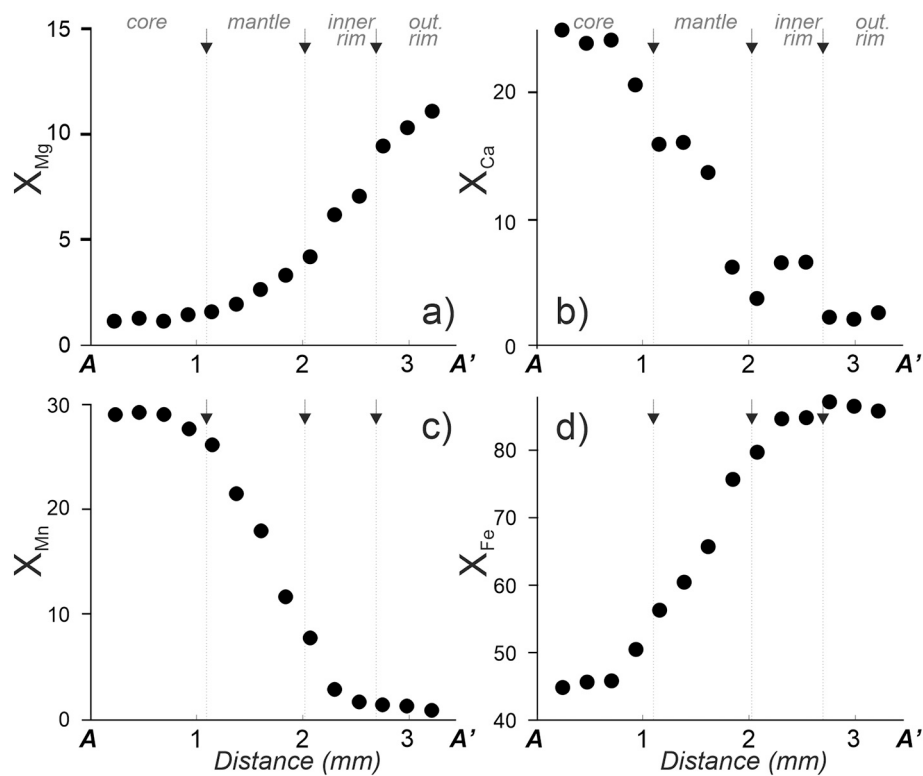
Fig. 3. Major element compositional profiles of Grt1. The compositional profile was acquired along the trace shown in the calcium map of Fig. 2.

Table 2

Trace elements and REE composition (μg/g) of the core, mantle, rim and outer rim of Grt1 and Grt2 from sample FZ13.

	Grt1									Grt2							
	core	core	core	mantle	annul.	inner rim	inner rim	out. rim	out. rim	core	core	core	mantle	inner rim	inner rim	out. rim	out. rim
Sc	221	221	215	103	286	45.5	47.6	45.6	46.8	143	143	101	92.3	74.9	27.8	26.7	18.1
Ti	1233	1157	1197	597	3626	524	457	230	217	167	167	134	320	62.9	64.8	39.2	36.9
V	93.6	84.3	89.4	37.9	63.9	62.1	45.3	16.3	35.5	88.6	99.8	77.8	42.1	64.1	48.6	48.3	43.3
Cr	88.2	93.7	120	123	120	50.1	57.4	68.1	119	84.4	95.9	74.6	62.7	70.9	6.2	145	136
Y	399	570	501	341	1391	110	101	42.4	2.11	474	393	299	262	91.9	55.5	5.11	4.42
Zr	20.0	19.5	19.9	11.3	54.5	4.62	2.87	3.09	2.91	5.04	20.1	19.8	15.0	4.09	4.41	2.84	2.84
Nb	6.10	3.77	21.1	1.04	22.3	0.33	0.35	0.12	0.25	8.53	7.35	6.19	0.72	0.15	0.13	0.04	bdl
Hf	1.47	0.76	0.42	2.36	0.38	0.18	0.07	0.03	0.05	0.43	0.80	0.63	0.15	0.19	bdl	0.07	bdl
Ta	1.79	1.14	2.67	0.32	0.17	0.11	0.08	0.03	0.02	1.88	1.45	1.60	0.15	0.08	0.06	bdl	0.03
Pb	5.21	4.73	4.25	6.10	22.4	0.65	bdl	0.02	0.02	3.12	2.84	2.25	1.63	0.59	0.34	0.02	0.01
Th	0.91	13.8	0.11	0.12	10.0	0.18	0.04	0.01	bdl	0.01	0.55	0.04	0.03	0.01	0.01	bdl	0.01
U	0.39	0.05	0.27	1.27	5.96	0.36	0.10	bdl	0.04	0.08	0.24	0.23	0.21	0.18	0.18	0.01	0.01
La	0.40	0.12	0.02	bdl	49.8	0.02	0.04	bdl	bdl	bdl	0.02	0.02	bdl	bdl	0.02	bdl	bdl
Ce	0.81	0.30	0.06	bdl	96.2	0.05	0.06	bdl	0.01	bdl	0.04	0.15	0.02	bdl	0.02	bdl	bdl
Pr	0.04	0.04	0.01	bdl	10.3	0.04	0.04	bdl	0.01	bdl	bdl	0.03	0.04	0.03	0.01	bdl	bdl
Nd	0.39	0.33	0.44	0.07	37.9	1.14	1.01	bdl	bdl	bdl	0.11	0.16	0.30	0.83	0.43	bdl	bdl
Sm	0.30	0.71	0.82	1.17	9.37	8.23	7.34	0.50	0.31	0.62	0.39	0.45	0.55	6.81	8.02	0.65	1.07
Eu	1.09	1.31	1.17	1.18	4.23	6.01	5.05	0.53	0.35	0.13	0.30	0.24	1.89	5.94	5.78	0.90	0.52
Gd	6.83	9.44	11.92	10.94	43.2	40.21	31.76	4.70	2.12	3.19	2.81	2.67	19.29	42.16	31.81	4.23	3.28
Tb	3.34	5.38	6.36	4.94	17.6	7.65	5.98	1.12	0.47	2.13	1.92	1.57	7.45	6.92	4.59	0.73	0.73
Dy	48.0	71.8	88.5	55.7	196	31.0	28.9	4.35	2.85	38.4	33.1	26.2	52.8	28.9	18.4	1.97	2.19
Ho	13.6	19.5	25.8	12.2	51.9	3.85	3.76	0.46	0.28	15.9	13.3	9.84	10.2	3.72	2.07	0.17	0.17
Er	51.5	68.2	93.9	35.5	168	6.90	7.12	1.13	0.35	76.8	61.3	42.7	25.3	5.85	3.60	0.33	0.39
Tm	8.75	10.7	14.9	5.32	22.0	0.76	0.71	0.08	0.02	16.5	14.0	9.45	3.43	0.62	0.45	0.06	0.03
Yb	67.1	79.0	111	32.9	132	4.30	3.70	0.41	0.27	152	135	81.8	19.4	2.99	1.60	0.35	0.47
Lu	10.4	11.5	16.6	4.54	17.2	0.33	0.36	0.15	0.08	24.1	22.2	12.7	2.14	0.39	0.24	0.11	0.06
ΣREE	213	278	371	164	856	110	95.8	13.4	7.11	330	284	188	143	105	77.1	9.50	8.91

HREE depletion in matrix during garnet growth (Hickmott and Spear, 1992; Otamendi et al., 2002). Rather, a HREE-rich core and an M-shaped distribution (central peak and lateral shoulders, Fig. 4) of MREE has been successfully modeled by Skora et al. (2006) as a diffusion-limited uptake process. This model assumes that a garnet nucleating in a matrix with a given REE budget incorporates REE as a function of their initial contents and their garnet/matrix partition coefficients, i.e. with a preference for the more compatible heavy and medium REE (central peaks in the profile).

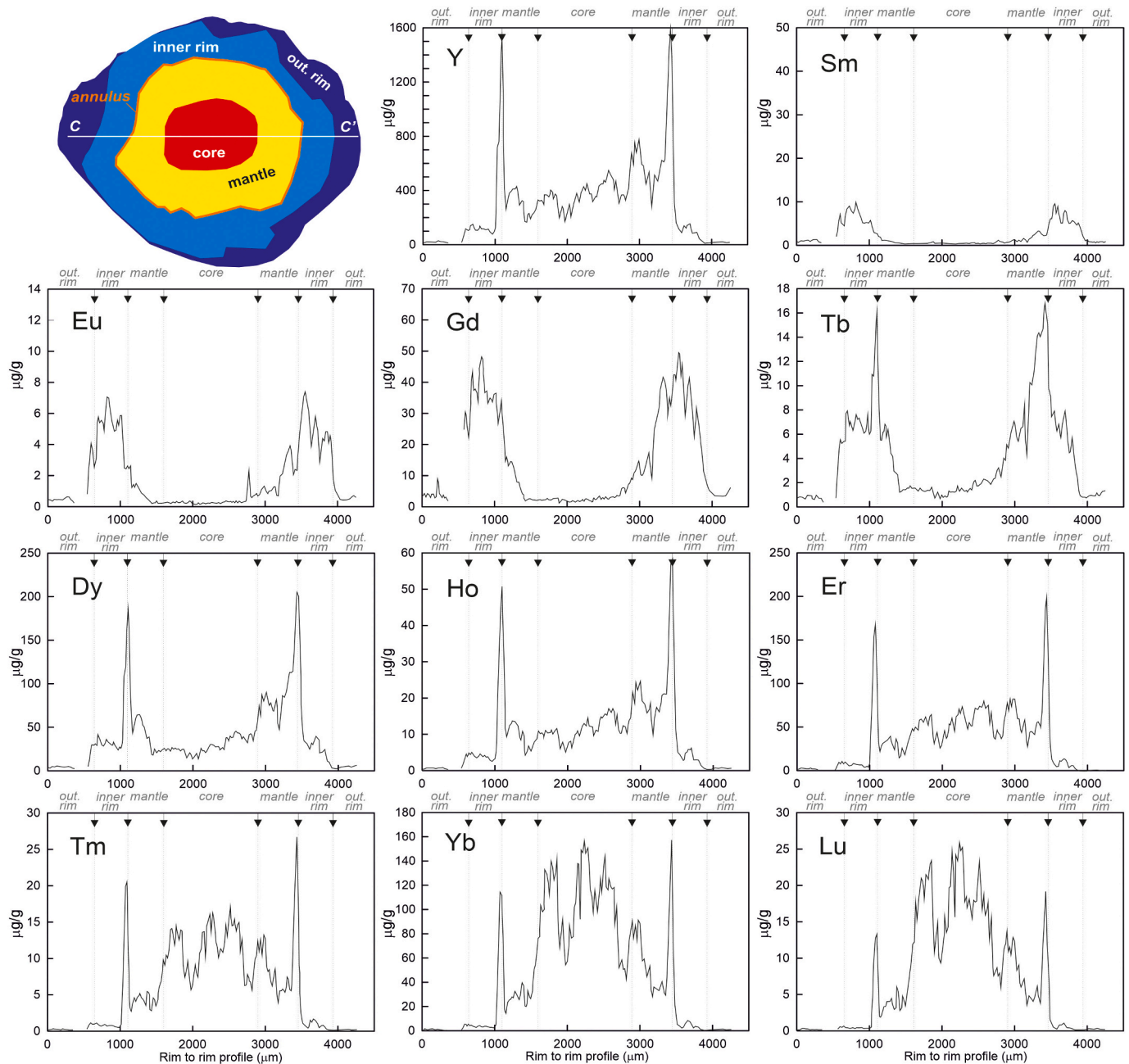The matrix surrounding the garnet becomes depleted in REE due to

Fig. 4. Trace elements compositional profiles (μg/g) of Grt1 along the C-C′ trace.

their low diffusivity, resulting in low incorporation into the garnet. The progressive increase in temperature, and decreasing pressure in stage (b) (see Fig. 8) leads to an increase in diffusivity and a new increase in REE uptake by garnet (namely, lateral peaks, or shoulders or second maxima in the profile). The diffusivity increase is more pronounced for elements with a smaller ionic radius, so that the larger LREE enter the garnet later than the smaller and faster diffusing HREE, explaining the progressive shift of the shoulders towards the rim as the atomic number decreases.

In the samples studied, this type of zoning occurs in the garnet core, mantle and inner rim, while the final stages of garnet growth occur in a depleted matrix documented by the REE-poor outer rim. Beside this general trend, there is also an asymmetric enrichment in the mantle zone, resulting in a broader and oscillating central peak in the profile. This could be due to irregularities in the shape of the initial garnet grain or local variations in the diffusivity of the REE in the matrix.

The rimwards increase in concentrations with decreasing REE atomic

number has been previously described in amphibolite- and eclogite-facies garnet (e.g. Fukushima et al., 2021; George et al., 2018; Moore et al., 2013; Skora et al., 2006), although it is not a ubiquitous feature (e. g. Rubatto et al., 2020) also because the diffusivity difference between light and heavy REE is expected to decrease with increasing temperature (e.g. Moore et al., 2013). The zoning in Grt1 fits well with this model of diffusion-limited uptake and supports that the different growth zones from core to rim grew in a seemly continuous, long-lasting evolution, despite the discontinuity in the garnet growth represented by the Y + REE *annulus* (see below).

6.2. Annular enrichment zone

The TE data and maps presented in this paper reveal the occurrence of an Y + HREE discontinuity at the mantle/rim transition (Figs. 4,5). However, the progressive outward migration of the REE-rich zone with
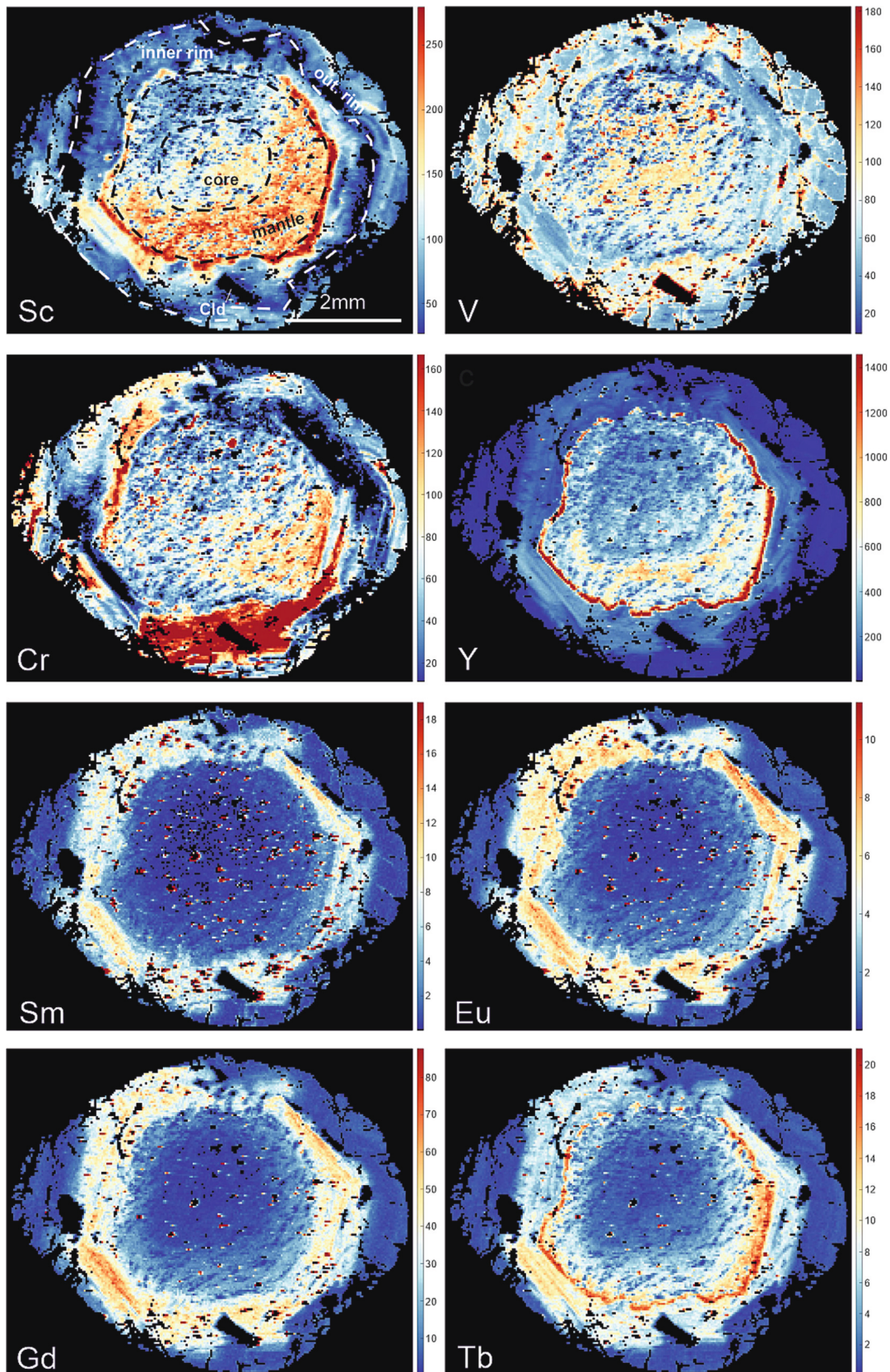
Fig. 5. LA-ICPMS concentration maps (μg/g) for selected trace elements of the Grt1 porphyroblast.
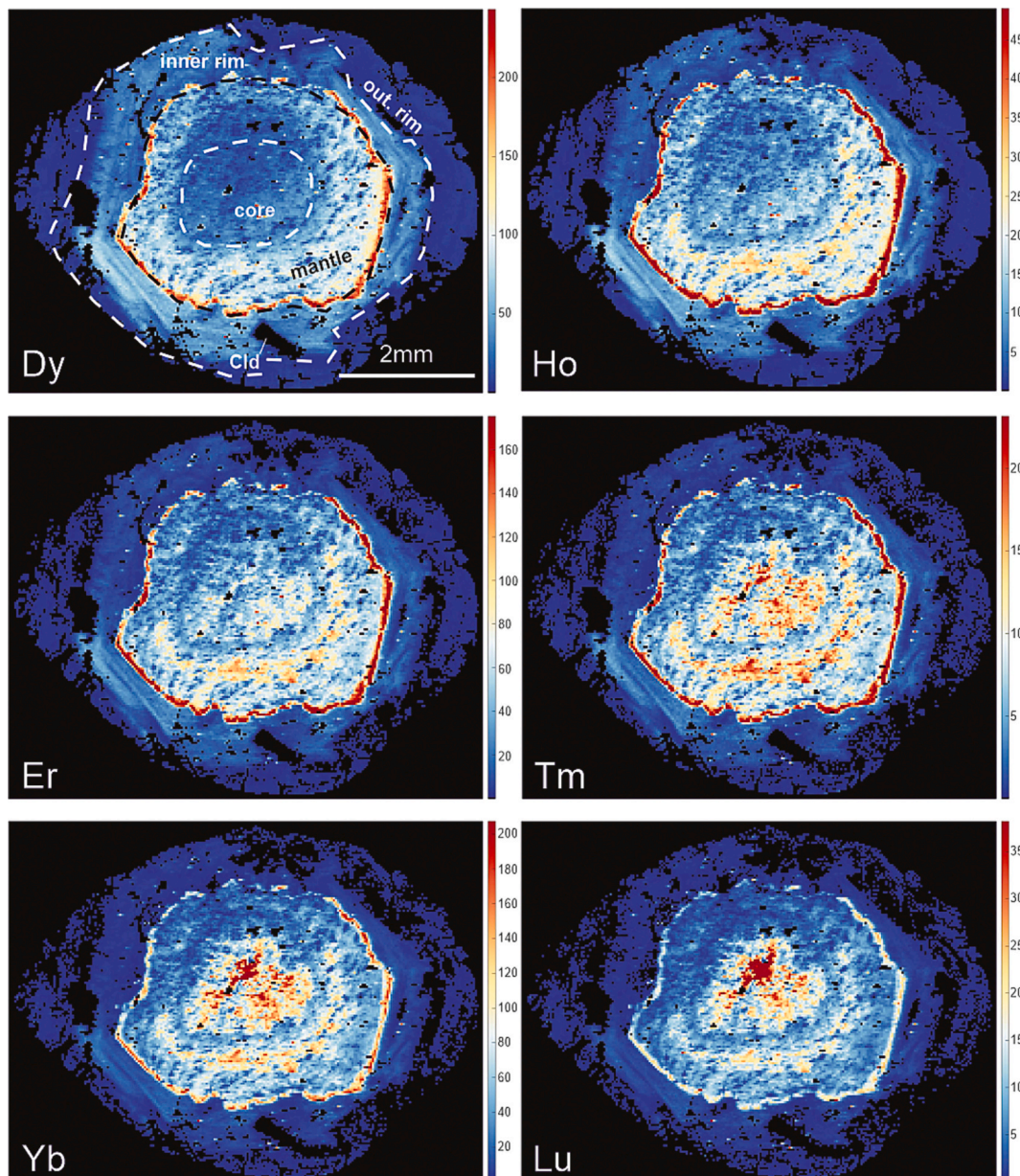
Fig. 5. (*continued*).

decreasing atomic number is not affected by the *annulus*, suggesting that the *annulus*-forming process was a short-lived episode in the relatively continuous and protracted garnet growth history.

High-Y annuli in garnet have previously been attributed to garnet resorption and renewed growth (Pyle and Spear, 1999), disequilibrium partitioning consequent to changing garnet growth rate (Chernoff and Carlson, 1999; Lanzirotti, 1995), breakdown of Y-enriched phases (Hickmott and Spear, 1992; Spear and Kohn, 1996). The lack of any Mn or Ca enrichment in the *annulus* (Fig. 2) which is a marker for garnet resorption and back diffusion (e.g. Giuntoli et al., 2018, Gaidies et al., 2021; Pyle and Spear, 1999, Kohn and Spear, 2000, Carlson, 2002), the generally euhedral shape of the *annulus* with no cross cutting relationships between growth zones before and after, and the symmetrical profile of the *annulus* are all evidences that extensive garnet resorption and regrowth did not play a relevant role in the *annulus*-forming process.

Besides, significant decrease in garnet growth rate is clearly testified by the garnet microstructure (Fig. 1) characterized by inclusion-rich core+mantle (formed during rapid garnet growth) and inclusion-free rims (reflecting slower growth rate). The studied garnet lacks any textural evidence of resorption (with the only exception of a discontinuous, anhedral margin visible at the top of the *annulus* in Fig. 5) as well as any evidence of breakdown of Y-enriched phases. The Y + HREE *annulus* at the mantle-rim boundary is interpreted here as resulting from a decrease in the growth rate of the crystal, similarly to what observed by Thakur et al. (2018) for a garnet grade metapelite from the Main Central Thrust Zone, NW Himalaya (see Fig. 5d in Thakur et al., 2018, pag.7). Decrease, or even stagnation, in garnet growth rate as a possible mechanism favoring REE enrichment was also proposed by Tual et al. (2022).

The occurrence of sharp annuli for specific TE in garnet has been attributed also to the breakdown of TE-rich major and/or accessory minerals during garnet growth (see, among others, Konrad-Schmolke et al., 2008; Raimondo et al., 2017; Bebout et al., 2022). However, although we cannot exclude the local, incidental supply provided by the breakdown of coexistent mineral phases, this last explanation seems to not apply well to our case study, since the annular enrichment does not represent a protracted event, such as the breakdown reaction of a coexistent mineral should be, in the garnet history.
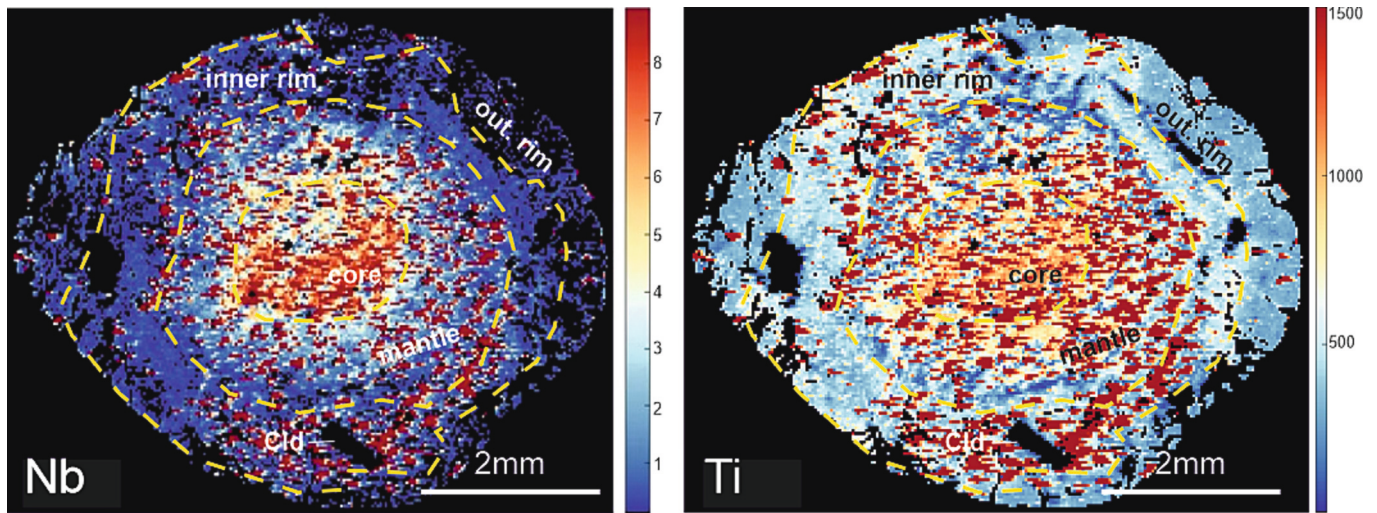
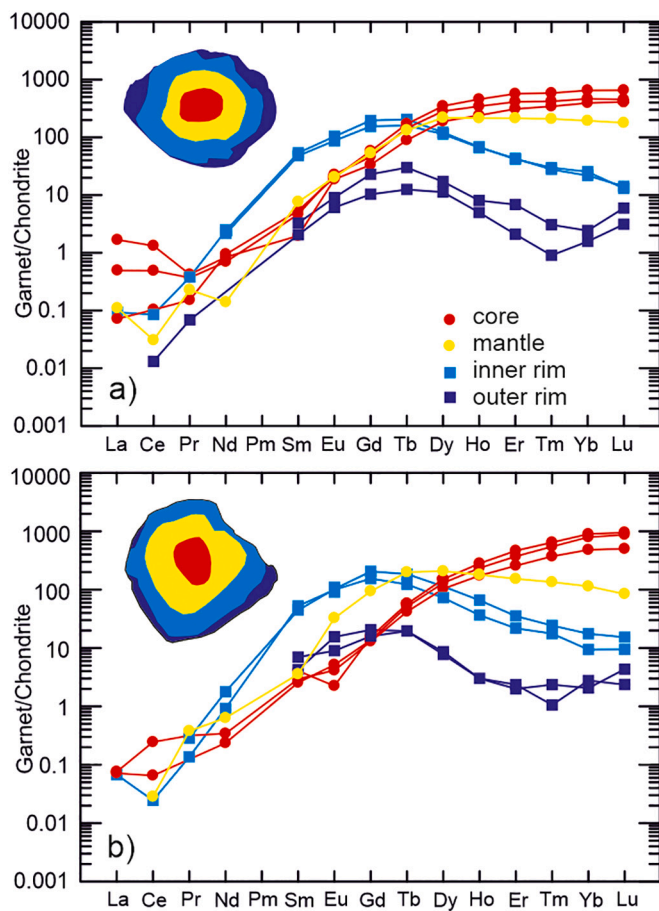**Fig. 6.** LA-ICPMS concentration maps (μg/g) for Nb and Ti of the Grt1 porphyroblast.

Fig. 7. REE patterns normalized to chondrite (McDonough and Sun, 1995) of core, mantle, inner rim and outer rim of Grt1 and Grt2.
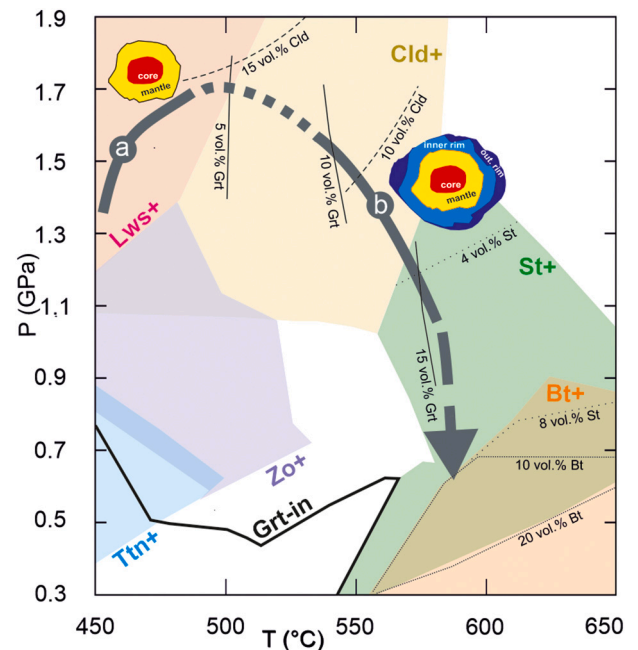

Fig. 8. P-T path (modified from Cruciani et al., 2022), calculated on the basis of the zoning of garnet major components by the CZGM software by Faryad and Ježek (2019), showing the garnet core + mantle prograde growth (solid line *a*) and the rim growth (solid line *b*) separated by a decrease, or even stagnation, in garnet growth (dotted line). The last part of the P-T path (dashed line) was drawn on the basis of the rock mineral assemblage, that includes St + Bt. The stability fields of titanite, zoisite, lawsonite, chloritoid, staurolite, biotite and garnet are also shown. Selected isomodes for garnet, chloritoid, staurolite and biotite are also shown.

Similar annular compositional discontinuities have been attributed to polyphase garnets (Gaidies et al., 2021). However, although the microstructural evidence (i.e. the transition between peciloblastic core+mantle vs. rim poor of inclusions) indicates a significant decrease in the garnet growth rate, it is difficult to evaluate if the two stages (rapid the first and slow the second) of garnet growth represent two different garnet generations. This aspect has to be further investigated, for

example with the help of Lu—Hf dating techniques. Until precise age constrains for each one of the different growth zones will be available, we could simply hypothesize that the two garnet growth events both belong to the Variscan metamorphism.

6.3. Trace element supply from other mineral phases

The depletion in almandine component of the inner part of the garnet shown in Fig. 2d is compatible with an initial garnet growth in equilibrium with chloritoid (i.e. iron-rich phase). On the other hand, the bell-

shaped trend of decreasing Ca towards the rim is an evidence that the inner part of the garnet grew by a continuous metamorphic reaction in which calcium was supplied to the garnet, from the breakdown of a Ca-rich phase. The extremely low concentrations of the MREE (Sm, Eu, Gd) in the core+mantle growth zone are also consistent with prograde growth of the garnet in coexistence with Ca-rich phases which are the main repositories of MREE in blueschist-facies rocks (Fukushima et al., 2021; Inui and Toriumi, 2004; Spandler et al., 2003). Among the Ca-rich silicate phases, epidote (or lawsonite) and titanite are all predicted to be stable along the prograde part of the P-T path of the sample studied (see Fig. A2, modified from Cruciani et al., 2022). Allanite was reported for adjacent rocks of the staurolite zone by Franceschelli et al. (2002). The occurrence of allanite in the staurolite zone (as well as in the other lower-grade metamorphic zones) of the metamorphic basement of Sardinia and its absence in the sample studied, suggests that this mineral may have decomposed during the prograde P-T path (most likely to form monazite, which was found as inclusions in garnet).

Besides the predominant compositional features (i.e. REE abundance controlled by atomic number + annular enrichment) of TE in garnet in the mylonitic micaschist, there are some additional variations in trace element concentrations that are better explained by local availability of elements and/or variability in transport mechanisms. Cr and V are slightly enriched in the garnet core+mantle domain with respect to the rim, and are not enriched in the *annulus*. However, they are enriched in an irregular domain cutting the rim around a chloritoid inclusion (Fig. 5). The chloritoid included in garnet of our sample is richer in Cr (42–78 μg/g) than in Sc (~ 6 μg/g) and does not contain MREE. We conclude that chloritoid had no influence on the Sc budget, and its breakdown was not responsible for the V and Cr zoning. We propose that the irregular distribution of V and Cr in the studied garnet is due to inheritance from lawsonite and/or epidote due to their slow diffusivity in the matrix compared to Sc, Y and HREE, which were instead redistributed and contributed to the enrichment in the *annulus*.

6.4. Reaction history

According to the observations reported above, it is possible to reconstruct the following reaction history reflected by the garnet growth zones and by the major and trace element compositional zoning.

Chloritoid and quartz inclusions observed in garnet porphyroblasts suggest that almandine and pyrope components in garnet formed through the reaction:

$$Cld + Chl + Qz = Grt + H_2O$$
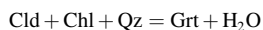
Franceschelli et al. (1982) documented that epidote is the main Ca source for the grossular forming reaction in metapelites of NE Sardinia. The nucleus of the garnet, which is enriched in Ca, Mn and garnet-compatible elements such as Sc, Y and HREE is thought to be possibly derived from the prograde decomposition of epidote and/or allanite according to a reaction similar to that proposed by Yang and Rivers (2002), without the contribution of K-bearing phases (i.e. K-white mica, biotite).

$$Chl + Ep = Grt + Pl + H_2O$$

The garnet rim contains significantly lower Ca, Mn and compatible elements consistent with their progressive depletion in the surrounding matrix. The presence of staurolite inclusions in the garnet rim, together with the assumption that high-Y annuli in staurolite-zone samples may result from prograde dissolution of garnet via the staurolite-in reaction (Kohn and Malloy, 2004; Pyle and Spear, 2003), seems to suggest that the garnet consumption possibly enhanced the staurolite formation according to the reaction:

$$Grt + Chl + Ms. = St + Bt + Qz + H_2O$$
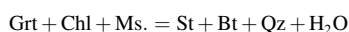
Finally, the flat patterns of major elements (Mg, Fe, Ca and Mn)

observed in the rim can supposed to be, at least in part and/or restricted to the outer rim itself, influenced by diffusion at temperatures close to 600 °C.

7. Concluding remarks

Major element and trace element mapping of the studied garnet shows that the TE zoning pattern is generally consistent with the four distinct growth zones (core, mantle, inner rim and outer rim) recognized on the basis of major element zoning. However, the TE have a more complex zoning than the bell-shaped pattern shown by the major elements and provide further insight into growth history of the garnet. The REE distribution, trend and behavior in the growth zones can mainly be explained by diffusion-limited REE uptake. The *annulus*, interpreted here as a decrease in garnet growth rate, reflects a short-lived episode in the relatively continuous and protracted garnet growth history.

Supplementary data to this article can be found online at https://doi.org/10.1016/j.lithos.2023.107436.

References

Baxter, E.F., Caddick, M.J., Dragovic, B., 2017. Garnet: a rock-forming mineral petrochronometer. Rev. Mineral. Geochem. 83, 469–533.

Bebout, G.E., Ota, T., Kunihiro, T., Carlson, W.D., Nakamura, E., 2022. Lithium in garnet as a tracer of subduction zone metamorphic reactions: the record in ultrahigh-pressure metapelites at Lago di Cignana, Italy. Geosphere 18 (3), 1020–1029.

Bovay, T., Rubatto, D., Lanari, P., 2021a. Pervasive fluid-rock interaction in subducted oceanic crust revealed by oxygen isotope zoning in garnet. Contrib. Mineral. Petrol. 176, 55.

Bovay, T., Lanari, P., Rubatto, D., Smit, M., Piccoli, F., 2021b. Pressure–temperature–time evolution of subducted crust revealed by complex garnet zoning (Theodul Glacier Unit, Switzerland). J. Metamorph. Geol. 40, 175–206.

Cao, D.D., Cheng, H., Zhang, L., 2017. Pseudosection modelling and garnet Lu–Hf geochronology of HP amphibole schists constrain the closure of an ocean basin between the northern and southern Lhasa blocks, Central Tibet. J. Metamorph. Geol. 35, 777–803.

Carlson, W.D., 2002. Scales of disequilibrium and rates of equilibration during metamorphism. Am. Mineral. 87, 185–204.

Carmignani, L., Oggiano, G., Barca, S., Conti, P., Eltrudis, A., Funedda, A., Pasci, S., Salvadori, I., 2001. Geologia della Sardegna (Note illustrative della Carta Geologica della Sardegna in scala 1:200000). Memorie descrittive della Carta Geologica d'Italia, vol. LX. Servizio Geologico Nazionale. Istituto Poligrafico e Zecca dello Stato, Roma, p. 283.

Carosi, R., Palmeri, R., 2002. Orogen-parallel tectonic transport in the Variscan belt of northeastern Sardinia (Italy): implications for the exhumation of medium-pressure metamorphic rocks. Geol. Mag. 139, 497–511.

Carosi, R., Petroccia, A., Iaccarino, S., Simonetti, M., Langone, A., Montomoli, C., 2020. Kinematics and timing constraints in a transpressive tectonic regime: the example of the Posada-Asinara Shear Zone (NE Sardinia, Italy). Geosciences 10, 288.

Chernoff, C.B., Carlson, W.D., 1999. Trace element zoning as a record of chemical disequilibrium during garnet growth. Geology 27, 555–558.

Connolly, J.A.D., Memmi, I., Trommsdorff, V., Franceschelli, M., Ricci, C.A., 1994. Forward modeling of calc-silicate microinclusions and fluid evolution in a graphitic metapelite, Northeast Sardinia. Am. Mineral. 79, 960–972.

Cruciani, G., Franceschelli, M., Langone, A., Puxeddu, M., Scodina, M., 2015. Nature and age of pre-Variscan eclogite protoliths from the Low- to Medium-Grade Metamorphic

complex of north–Central Sardinia (Italy) and comparisons with coeval Sardinian eclogites in the northern Gondwana context. J. Geol. Soc. Lond. 172, 792–807.

Cruciani, G., Franceschelli, M., Massone, H.-J., Musumeci, G., Spano, M.E., 2016. Thermomechanical evolution of the high-grade core in the nappe zone of Variscan Sardinia, Italy: the role of shear deformation and granite emplacement. J. Metamorph. Geol. 34, 321–342.

Cruciani, G., Franceschelli, M., Puxeddu, M., Tiepolo, M., 2018. Metavolcanics from Capo Malfatano, SW Sardinia, Italy: new insight on the age and nature of Ordovician volcanism in the Variscan foreland zone. Geol. J. 53, 1573–1585.

Cruciani, G., Fancello, D., Franceschelli, M., Musumeci, G., 2019. Geochemistry of the Monte Filau orthogneiss (SW Sardinia, Italy): insight into the geodynamic setting of Ordovician felsic magmatism in the N/NE Gondwana margin. Ital. J. Geosci. 138, 136–152.

Cruciani, G., Franceschelli, M., Massone, H.-J., Musumeci, G., 2021. Evidence of two metamorphic cycles preserved in garnet from felsic granulite in the southern Variscan belt of Corsica, France. Lithos 380–381, 105919.

Cruciani, G., Franceschelli, M., Carosi, R., Montomoli, C., 2022. P-T path from garnet zoning in pelitic schist from NE Sardinia, Italy: further constraints on the metamorphic and tectonic evolution of the North Sardinia Variscan belt. Lithos 428–429, 106836.

Di Vincenzo, G., Carosi, R., Palmeri, R., 2004. The relationship between tectono-metamorphic evolution and argon isotope records in white mica: constraints from in situ 40Ar–39Ar laser analysis of the Variscan basement of Sardinia. J. Petrol. 45, 1013–1043.

Fancello, D., Cruciani, G., Franceschelli, M., Massone, H.-J., 2018. Trondhjemitic leucosomes in paragneisses from NE Sardinia: geochemistry and P-T conditions of melting and crystallization. Lithos 304-307, 501–517.

Faryad, S.W., Ježek, J., Connoly, J.A.D., 2019. Compositional zoning in garnet and its modification by diffusion during pressure and temperature changes in metamorphic rocks; an approach and software. Lithos 332–333, 287–295.

Faryad, S.W., Ježek, J., Connoly, J.A.D., 2022. Advantages and limitations of combined diffusion-phase equilibrium modelling for pressure–temperature–time history of metamorphic rocks. J. Petrol. 63, 1–19.

Ferry, J.M., Spear, F.S., 1978. Experimental calibration of the partitioning of Fe and Mg between biotite and garnet. Contrib. Mineral. Petrol. 66, 113–117.

Franceschelli, M., Memmi, I., Ricci, C.A., 1982. Ca distribution between garnet and plagioclase in pelitic and psammitic schists from the metamorphic basement of North-Eastern Sardinia. Contrib. Mineral. Petrol. 80, 285–295.

Franceschelli, M., Memmi, I., Ottolini, L., Vannucci, R., 2002. Trace- and major-element zoning in garnet: a case study in the pelitic schists of NE Sardinia (Italy). N. Jb. Miner. Mh. 8, 337–351.

Fukushima, R., Tsujimori, T., Aoki, S., Aoki, K., 2021. Trace-element zoning patterns in porphyroblastic garnets in low-T eclogites: parameter optimization of the diffusion-limited REE-uptake model. Island Arc 30, e12394.

Gaidies, F., Morneau, Y.E., Petts, D.C., Jackson, S.E., Zagorevski, A., Ryan, J.J., 2021. Major and trace element mapping of garnet: unravelling the conditions, timing and rates of metamorphism of the Snowcap assemblage, west-Central Yukon. J. Metamorph. Geol. 39, 133–164.

George, F.R., Gaidies, F., Boucher, B., 2018. Population-wide garnet growth zoning revealed by LA-ICP-MS mapping: implications for trace element equilibration and syn-kinematic deformation during crystallisation. Contrib. Mineral. Petrol. 173, 74.

Gieré, R., Rumble, D., Günther, D., Connolly, J.A.D., Caddick, M.J., 2011. Correlation of growth and breakdown of major and accessory minerals in metapelites from Campolungo, Central Alps. J. Petrol. 52, 2293–2334.

Giuntoli, F., Lanari, P., Engi, M., 2018. Deeply subducted continental fragments – part 1: fracturing, dissolution–precipitation, and diffusion processes recorded by garnet textures of the central Sesia Zone (western Italian Alps). Solid Earth 9, 167–189.

Griffin, W., Powell, W., Pearson, N., O'Reilly, S., 2008. GLITTER: data reduction software for laser ablation ICP-MS. Laser Ablation-ICP-MS in the earth sciences. Mineral. Assoc. Canada Short Course Ser. 40, 204–207.

Helbing, H., Tiepolo, M., 2005. Age determination of Ordovician magmatism in NE Sardinia and its bearing on Variscan basement evolution. J. Geol. Soc. Lond. 162, 689–700.

Helbing, H., Frisch, W., Bons, P.D., 2006. South Variscan terrane accretion: Sardinian constraints on the intra-Alpine Variscides. J. Struct. Geol. 28, 1277–1291.

Hickmott, D.D., Spear, F.S., 1992. Major- and trace-element zoning in garnets from calcareous pelites in the NW Shelburne Falls quadrangle, Massachusetts: garnet growth histories in retrograded rocks. J. Petrol. 33, 965–1005.

Higashino, F., Rubatto, D., Kawakami, T., Bouvier, A.-S., Baumgartner, L.P., 2019. Oxygen isotope speedometry in granulite facies garnet recording fluid/melt–rock interaction (Sør Rondane Mountains, East Antarctica). J. Metamorph. Geol. 37, 1037–1048.

Hirsch, D.M., Prior, D.J., Carlson, W.D., 2003. An overgrowth model to explain multiple, dispersed high-Mn regions in the cores of garnet porphyroblasts. Am. Mineral. 88, 131–141.

Inui, M., Toriumi, M., 2004. A theoretical study on the formation of growth zoning in garnet consuming chlorite. J. Petrol. 45 (7), 1369–1392.

Kohn, M.J., Malloy, M.A., 2004. Formation of monazite via prograde metamorphic reactions among common silicates: implications for age determinations. Geochim. Cosmochim. Acta 68 (1), 101–113.

Kohn, M.J., Spear, F.S., 2000. Retrograde net transfer reaction insurance for pressure-temperature estimates. Geology 28, 1127–1130.

Konrad-Schmolke, M., Zack, T., O'Brien, P.J., Jacob, D.E., 2008. Combined thermodynamic and rare earth element modelling of garnet growth during subduction: examples from ultrahigh-pressure eclogite of the Western Gneiss Region, Norway. Earth Planet. Sci. Lett. 272 (1–2), 488–498.

Konrad-Schmolke, M., Halama, R., Chew, D., Heuzé, C., De Hoog, J., Ditterova, H., 2023. Discrimination of thermodynamic and kinetic contributions to the heavy rare earth element patterns in metamorphic garnet. J. Metamorph. Geol. 41, 465–490.

Kulhánek, J., Faryad, S.W., 2023. Compositional changes in garnet: trace element transfer during eclogite-facies metamorphism. Contrib. Mineral. Petrol. 178, 68.

Kulhánek, J., Faryad, S.W., Jedlicka, R., Svojtka, M., 2021. Dissolution and reprecipitation of garnet during eclogite-facies metamorphism; major and trace element transfer during atoll garnet formation. J. Petrol. 62 (11), 1–22.

Lanari, P., Piccoli, F., 2020. New horizons in quantitative compositional mapping–Analytical conditions and data reduction using XMapTools. In: IOP Conference Series: Materials Science and Engineering, vol. 891, No. 1. IOP Publishing, p. 012016.

Lanzirotti, A., 1995. Yttrium zoning in metamorphic garnets. Geochim. Cosmochim. Acta 59, 4105–4110.

Massone, H.-J., Cruciani, G., Franceschelli, M., Musumeci, G., 2018. Anticlockwise pressure–temperature paths record Variscan upper-plate exhumation: example from micaschists of the Porto Vecchio region, Corsica. J. Metamorph. Geol. 36, 55–77.

McDonough, W.F., Sun, S.S., 1995. The composition of the Earth. Chem. Geol. 120, 223–253.

Millonig, L.J., Albert, R., Gerdes, A., Avigad, D., Dietsch, C., 2020. Exploring laser ablation U–Pb dating of regional metamorphic garnet – The Straits Schist, Connecticut, USA. Earth Planet. Sci. Lett. 552, 116589.

Moore, S.J., Carlson, W.D., Hesse, M.A., 2013. Origins of yttrium and rare earth element distributions in metamorphic garnet. J. Metamorph. Geol. 31, 663–689.

Otamendi, J.E., de la Rosa, J.D., Patiño Douce, A.E., Castro, A., 2002. Rayleigh fractionation of heavy rare earths and yttrium during metamorphic garnet growth. Geology 30, 159–162.

Page, F.Z., Essene, E.J., Mukasa, S.B., Valley, J.W., 2014. A garnet-zircon oxygen isotope record of subduction and exhumation fluids from the Franciscan complex, California. J. Petrol. 55 (1), 103–131.

Pollington, A.D., Baxter, E.F., 2011. High precision microsampling and preparation of zoned garnet porphyroblasts for Sm–Nd geochronology. Chem. Geol. 281, 270–282.

Pyle, J.M., Spear, F.S., 1999. Yttrium zoning in garnet: coupling of major and accessory phases during metamorphic reactions. Geol. Mater. Res. 1, 1–49.

Pyle, J.M., Spear, F.S., 2003. Yttrium zoning in garnet: coupling of major and accessory phases during metamorphic reactions. Am. Mineral. 88 (4), 708.

Raimondo, T., Clark, C., Hand, M., Cliff, J., Harris, C., 2012. High-resolution geochemical record of fluid-rock interaction in a mid-crustal shear zone: a comparative study of major element and oxygen isotope transport in garnet. J. Metamorph. Geol. 30 (3), 255–280.

Raimondo, T., Payne, J., Wade, B., Lanari, P., Clark, C., Hand, M., 2017. Trace element mapping by LA-ICP-MS: assessing geochemical mobility in garnet. Contrib. Mineral. Petrol. 172, 17.

Rubatto, D., Burger, M., Lanari, P., Hattendorf, B., Schwarz, G., Neff, C., Keresztes Schmidt, P., Hermann, J., Vho, A., Günther, D., 2020. Identification of growth mechanisms in metamorphic garnet by high-resolution trace element mapping with LA-ICP-TOFMS. Contrib. Mineral. Petrol. 175, 61.

Scodina, M., Cruciani, G., Franceschelli, M., Massone, H.-J., 2019. Anticlockwise P-T evolution of amphibolites from NE Sardinia, Italy: geodynamic implications for the tectonic evolution of the Variscan Corsica-Sardinia block. Lithos 324, 763–775.

Scodina, M., Cruciani, G., Franceschelli, M., Massone, H.-J., 2020. Multilayer corona textures in the high-pressure ultrabasic amphibolite of Mt. Nieddu, NE Sardinia (Italy): Equilibrium versus disequilibrium. Per. Miner. 89, 169–186.

Scodina, M., Cruciani, G., Franceschelli, M., 2021. Metamorphic evolution and P–T path of the Posada Valley amphibolites: new insights on the Variscan high pressure metamorphism in NE Sardinia, Italy. C.R. Geosci. 353 (1), 227–246.

Seman, S., Stockli, D.F., McLean, N.M., 2017. U-Pb geochronology of grossular-andradite garnet. Chem. Geol. 460, 106–116.

Simpson, A., Gilbert, S., Tamblyn, R., Hand, M., Spandler, C., Gillespie, J., Nixon, A., Glorie, S., 2021. In-situ Lu-Hf geochronology of garnet, apatite and xenotime by LA ICP MS/MS. Chem. Geol. 577, 120299.

Simpson, A., Glorie, S., Hand, M., Spandler, C., Gilbert, S., 2023. Garnet Lu-Hf speed dating: a novel method to rapidly resolve polymetamorphic histories. Gondwana Res. 121, 215–234.

Skora, S., Baumgartner, L.P., Mahlen, N.J., Johnson, C.M., Pilet, S., Hellebrand, E., 2006. Diffusion-limited REE uptake by eclogite garnets and its consequences for Lu–Hf and Sm–Nd geochronology. Contrib. Mineral. Petrol. 152, 703–720.

Smit, M.A., Scherer, E.E., Mezger, K., 2013. Lu–Hf and Sm–Nd garnet geochronology: chronometric closure and implications for dating petrological processes. Earth Planet. Sci. Lett. 381, 222–233.

Spandler, C., Hermann, J., Arculus, R., Mavrogenes, J., 2003. Redistribution of trace elements during prograde metamorphism from lawsonite blueschist to eclogite facies; implications for deep subduction-zone processes. Contrib. Mineral. Petrol. 146, 205–222.

Spear, F.S., Kohn, M.J., 1996. Trace element zoning in garnet as a monitor of crustal melting. Geology 24, 1099–1102.

Thakur, S.S., Madhavan, K., Patel, S.C., Rameshwar Rao, D., Singh, A.K., Pandey, S., Nandini, P., 2018. Yttrium-zoning in garnet and stability of allanite in metapelites from the Main Central Thrust Zone and adjacent higher Himalayan crystallines along the Alaknanda Valley, NW Himalaya. Lithos 320–321, 1–19.

Thiessen, E.J., Gibson, H.D., Regis, D., Pehrsson, S.J., Ashley, K.T., Smit, M.A., 2019. The distinct metamorphic stages and structural styles of the 1.94–1.86 Ga Snowbird Orogen, Northwest Territories, Canada. J. Metamorph. Geol. 38, 963–992.

Tual, L., Smit, M.A., Cutts, J., Kooijman, E., Kielman-Schmitt, M., Majka, J., Foulds, I., 2022. Rapid, paced metamorphism of blueschists (Syros, Greece) from laser-based

zoned Lu-Hf garnet chronology and LA-ICPMS trace element mapping. Chem. Geol. 607, 121003.

Whitney, D.L., Evans, B.W., 2010. Abbreviations for names of rock-forming minerals. Am. Mineral. 95, 185–187.

Wu, C.-M., Cheng, B.-H., 2006. Valid garnet–biotite (GB) geothermometry and garnet–aluminum silicate–plagioclase–quartz (GASP) geobarometry in metapelitic rocks. Lithos 89, 1–23.

Yang, P., Rivers, T., 2002. The origin of Mn and Y annuli in garnet and the thermal dependence of P in garnet and Y in apatite in calc-pelite and pelite, Gagnon terrane, western Labrador. Geol. Mater. Res. 4 (1), 1–35.